ACS APPLIED ELECTRONIC MATERIALS

pubs.acs.org/acsaelm Article

Self-Powered Ion Sensing Using Two-Dimensional Biotite

Sumit Kumar,[#] Kleuton A. L. Lima,[#] Raphael M. Tromer, Dipanwita Mitra, Saswata Goswami, Surbhi Slathia, Marcelo L. Pereira Junior, Michael E. McConney, Ajit K. Roy, Saikat Talapatra, Mauricio Terrones, Douglas S. Galvão,* and Chandra Sekhar Tiwary*

Cite This: *ACS Appl. Electron. Mater.* 2026, 8, 5750−5762 Read Online

ACCESS | Metrics & More | Article Recommendations | Supporting Information

ABSTRACT: The autonomous and real-time ion monitoring in wearables demands sustainable materials capable of self-powered and ion sensing (especially Na and K). The alteration of such ions causes severe health issues such as neurological dysfunction, cardiac arrhythmias, or metabolic disorders. Here, we introduce 2D biotite as a natural multifunctional material that unifies ion sensing and energy harvesting in a single material platform. The surface charges and high surface-to-volume ratio of 2D biotite make it highly sensitive and selective to electrolytes ions. The 2D biotite-based flexible TENG generated output voltages ranging from ±10.4 to ±24.3 V over a frequency range of 1–10 Hz and 1–6 V human-motion harvesting, confirming wearable self-powered capability. Density functional theory and non-equilibrium Green's function simulations validated the performance hierarchy based on adsorption energetics and charge transfer. The current–voltage curves demonstrate that simulation results reproduce the same trend observed experimentally. The sequence follows NaOH/biotite > KOH/biotite > NaCl/biotite > KCl/biotite > $CaCl_2$/biotite > pure biotite, as seen in the experimental data as well. The work positions natural 2D biotite as a scalable, tunable, and eco-benign platform for next-generation self-powered smart wearable systems with multiple applications ranging from medical diagnostics to ion sensing and efficient energy generators.

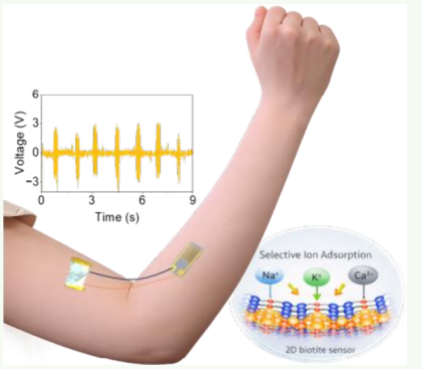

KEYWORDS: *2D biotite, ion sensing, self-powered, triboelectric nanogenerator, sustainable materials*

1. INTRODUCTION

Electrolytes and alkaline compounds such as sodium chloride (NaCl), potassium chloride (KCl), calcium chloride ($CaCl_2$), sodium hydroxide (NaOH), and potassium hydroxide (KOH) are of great importance in biological, environmental, and industrial systems, making their detection highly significant.[1,2] In the healthy human body, natural levels of sodium, potassium, and calcium ions are desirable since any imbalance can cause severe health issues, such as hyponatremia, hyperkalemia, or hypocalcemia, which may lead to neurological dysfunctions, cardiac arrhythmias, or metabolic disorders.[2−4] Typical ranges for normal serum sodium is 135–145 mEq/L, potassium is 3.5–5.0 mmol/L, and calcium is 2.2–2.6 mmol/L, Environmentally, chloride ions derived from NaCl, KCl, and $CaCl_2$ strongly influence water quality, and concentrations above the recommended 250 mg/L limit in drinking water (U.S. EPA) cause taste problems, corrosion of infrastructure, and ecological imbalance, emphasizing the need for accurate chloride monitoring.[5−8] Industrially, hydroxide ions from alkali hydroxide create highly alkaline conditions (pH > 12) in processes such as chemical synthesis, wastewater treatment, and food production, where uncontrolled levels can damage equipment, endanger workers, and harm ecosystems.[9,10] Therefore, the development of accurate, sensitive, and reliable sensors for the detection of NaOH, KOH, NaCl, KCl, and $CaCl_2$ is not only crucial for advancing diagnostics and safeguarding human health, but also for ensuring environmental sustainability and maintaining safe and efficient processes used in industrial operations.

Conventional sensing technologies, such as electrochemical (Ion-Selective Electrodes (ISE), Potentiometric sensors, and Amperometric sensors), optical (Surface Plasmon Resonance, fluorescence), and semiconductor-based (Ion-Sensitive Field-Effect Transistors (ISFET), Electric Double-Layer Field-Effect Transistors) have achieved promising sensitivity, yet each faces translational bottlenecks. [11,12] ISE membranes can quickly degrade, and are not favorable for miniaturization;[13−15] ISFETs require reference integration and anti-fouling engineering;[16] optical platforms rely on complex optics unsuitable for developing advanced wearables diagnostics systems;[17] and most nanomaterial-based sensors still rely on an external power

Received: April 16, 2026
Revised: June 15, 2026
Accepted: June 16, 2026
Published: July 2, 2026

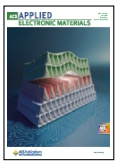

source, such as batteries, for their operation.[18] These are some of the fundamental challenges in the existing technology that create serious constraints in the development and long-term deployment of multifunctional sensors in implantable or infrastructure-free environments.[19] Many of these challenges can be met by utilizing intrinsic materials properties that can lead to a self- powered ion sensor in which the same material simultaneously performs ion recognition, charge transduction, and power generation, thus eliminating the need for external power sources and enabling closed-loop autonomous sensing.[20−22] Flexible triboelectric nanogenerators (TENG) provide a promising direction for harvesting biomechanical and ambient mechanical energy to support self-powered sensing.[23] Existing TENG-sensor hybrids adopt two different material architectures: a triboelectric layer for energy generation and a separate ion-selective layer for sensing. This segregation introduces interfacial mismatch, higher system complexity, parasitic losses, and weak signal coupling between ionic activity and triboelectric charge flow. Thus, there is a need for a multifunctional material that can harvest energy and electronically convert it to ions, allowing directly coupled, self-powered ion sensing. Here, we show that, utilizing Biotite [$K(Mg, Fe)_3(AlSi_3O_{10})$ $(OH, F, Cl)_2$], a layered phyllosilicate of the mica group whose unique structural, electrochemical, and physicochemical properties make it suitable for dual-functional applications, which can be utilized as a self-powered, wearable ion sensing system with possible applications in medical diagnostics.[23−27]

Biotite has a tetrahedral–octahedral–tetrahedral (TOT) type lamellar structure, in which Fe^{2+}/Mg^{2+}-rich octahedral sheets are sandwiched between silicate-based tetrahedral layers, while the interlayer K^+ ions are only weakly bound by van der Waals forces.[23,25,28] This structure makes it highly amenable to dissociation into 2D nanosheets via liquid-phase exfoliation, resulting in a large number of open active surface sites.[29] The –OH/–F functional groups and interlayer cation-exchange sites on the surface of exfoliated 2D biotite provide high affinity for Na^+, K^+, and Ca^{2+} ions, thus enabling selective ion adsorption and intercalation.[30−32] Its inherent negative surface charge and moderate dielectric constant ($\varepsilon_r \approx 6–8$) enable ion-induced charge redistribution with low leakage current.[29,33] Additionally, its interlayer ion diffusion coefficient ($D_i \approx 10^{-11}$ -10^{-13} cm^2 s^{-1}) enables more efficient electro-ionic transport than conventional synthetic ion-exchange membranes.[34] Its chemical stability make it suitable for long-term and harsh operating conditions.[30,35] All these properties make 2D biotite a unique natural material capable of simultaneously supporting ion-sensing and triboelectric voltage generation, a key requirement for the development of self-powered ion-sensing systems.

We introduce a biotite-based self-powered ion sensing platform in which exfoliated 2D biotite nanosheets function simultaneously as both the ion-responsive sensing layer (NaOH, KOH, NaCl, KCl, $CaCl_2$) and the triboelectric energy-harvesting layer in a biotite-TENG. Through controlled ion intercalation and surface functionalization, we can systematically tune interlayer spacing, defect states, and charge distribution within biotite, thus enabling direct modulation of both ionic sensing performance and triboelectric output. Pristine biotite delivers ±10.4 to ±24.3 V at a frequency range (f = 1–10 Hz), uniquely enabling direct LED illumination, and 1–6 V human-motion harvesting, confirming a unique wearable self-powered capability. Under human motion, ionic functionalization further tailors output amplitude and baseline potential, enabling direct powering of sensing operations without external electronics. The use of a single material for dual roles results in a material-synchronized self-powered architecture, in which the energy harvested from biomechanical or ambient motion is directly supplied to the biotite sensor for real-time ion detection.

2. EXPERIMENTAL SECTION

2.1. Exfoliation of 2D Biotite

A liquid chemical phase exfoliation technique was used to obtain 2D sheets from bulk biotite [$K(Mg, Fe)_3(Si_3AlO_{10})$ $(OH, F, Cl)_2$]. In this process, 100 mg of bulk biotite powder is exfoliated in 60 mL of isopropyl alcohol (IPA) at ambient temperature using a Rivotek probe sonicator for 18 h. To minimize possible contamination originating from the probe during prolonged sonication, the sonicator tip was thoroughly cleaned with ethanol and deionized water before and after each use. Sonication was performed under controlled power and pulse conditions to avoid mechanical erosion of the probe. No visible wear of the probe tip was observed after exfoliation. Thereafter, the exfoliated flakes were left undisturbed for over 24 h in order for the heavier flakes to precipitate at the bottom of the container. The dispersed fraction of the sample was used for further investigation.[23,25]

2.2. Sensor Device Fabrication

A 20 × 10 mm flexible Polyethylene Terephthalate (PET) substrate, printed with Cu (12 μm) / Ni (1μm)/ Au(1μm) interdigital electrode (IDE) on a 75 μm thick substrate (purchased from Newvision1981, Hong Kong, China), was used for the sensor device. The IDEs used have feature sizes with a line width of 100 μm, a line gap of 100 μm, and consist of 30 interdigitated fingers. Exfoliated 2D biotite sheets dispersed fraction in IPA were deposited on the interdigitated electrodes via drop-casting in steps of 5 μL droplets to form a uniform layer, upon drying, covering the electrodes. The process of the drying was continuously monitored for detectable currents. We estimate that the devices with ∼80 μL (16 droplets) of the deposited materials produced a current of ∼170 nA units under the application of 5 V. For sensing measurements, surface functionalization of the 2D biotite films was achieved by treating the deposited materials with different electrolytes and alkaline solutions of varying concentrations. 0.1 M solutions of NaCl (58 mg), KCl (75 mg), NaOH (40 mg), KOH (56 mg), and $CaCl_2$ (111 mg; anhydrous) were prepared by dissolving the respective salts in 10 mL of deionized (DI) water. After drop-casting, the devices were dried at room temperature to ensure stable immobilization of the functionalizing species. The fabricated bare and functionalized devices were then subjected to electrical characterization. Current–voltage (I–V) measurements were performed to investigate the effect of electrolyte and alkaline functionalization on the charge transport properties of the 2D biotite-based devices.

2.3. TENG Device Fabrication

A vertical contact–separation mode flexible TENG was designed and fabricated using a multilayer configuration, arranged from top to bottom, as follows: Aluminium (top electrode)/Kapton tape (tribo-negative layer)/Air gap/2D Biotite on PET (tribo-positive layer and substrate)/Aluminium (bottom electrode)/Kapton tape (insulating and supporting layer). A 4 cm^2 Kapton sheet was first laminated with an aluminium layer to form the top electrode. Kapton tape serves as the tribo-negative layer, generating electrons during contact–separation, while the aluminium film functions as the conductive electrode for efficient charge transfer and signal collection. The bottom triboelectric unit was fabricated by drop-casting 2D biotite sheets (1000 μL dispersion) onto a 4 cm^2 PET substrate and drying under ambient conditions to form a uniform layer. 2D biotite acts as a tribo-positive surface due to its high surface polarity, layered silicate

https://doi.org/10.1021/acsaelm.6c00747
ACS Appl. Electron. Mater. 2026, 8, 5750−5762

structure, and natural cationic sites that help attract electrons. PET provides mechanical flexibility and structural support. The aluminum layer beneath the PET acts as the bottom electrode, while the Kapton tape applied to the base acts as an insulating protective layer, reducing charge leakage and improving mechanical stability. The top and bottom assemblies were aligned face-to-face with a controlled air gap between the Kapton and 2D biotite surface to enable repeated contact–separation under mechanical stress. Copper wires were used to connect both Al electrodes externally for electrical measurements.

2.4. Characterization

The phase identification of bulk and 2D biotite was carried out using X-ray diffraction (XRD) (Bruker D8 Advance) with Cu Kα radiation of wavelength λ = 0.15406 nm. All the Raman spectroscopic study and Raman mapping were performed using a WITec UHTS Raman spectrometer (WITec, UHTS 300 VIS, Germany) with a 532 nm laser source and 17 mW laser power, using a 1800 lines/mm grating in 2 s integration time and 10 accumulations for each data point. The atomic orientation of the 2D flakes was investigated using a Transmission Electron Microscope, in High Angle Annular Dark Field (TEM-HAADF) (Jeol, F30, FEI) operating at 300 kV. The FTIR study was performed using a FTIR spectrometer, NICOLET 6700 model (Thermofisher Scientific Instruments) in transmission mode with KBr pellets as sample support substrates. The surface elemental composition and chemical states of the samples were analyzed using a PHI 5000 VersaProbe III scanning X-ray photoelectron spectroscopy (XPS) microprobe. The zeta potential of the samples was analyzed using an Anton Paar Litesizer 500 particle analyzer. The current–voltage (*I*–*V*) characteristics and gas-sensing measurements were carried out using a Keithley 2450 SourceMeter (Keithley Instruments, USA).

2.5. Computational Methods

First-principles calculations were carried out to investigate, at the atomic level, the mechanisms of adsorption, charge redistribution, and electronic transport underlying ionic modulation in 2D biotite surfaces in the presence of small ionic species of physicochemical and technological relevance. The systems included chlorides (NaCl, KCl, and $CaCl_2$) and alkali hydroxides (NaOH and KOH), which exhibit distinct dissociation and polarity behaviors,[36] allowing a comparative evaluation of ion-surface coupling mechanisms that govern ionic conduction and the electrical response of silicate-based layered materials. All calculations were performed using the DMol^3 package based on DFT,[37] which employs numerical radial basis functions for atomic orbital representation. This approach was applied to optimize the geometries of both isolated molecules and adsorbed configurations. Spin polarization was included throughout to ensure accurate total energies and account for potential local magnetic variations. Exchange-correlation effects were treated within the Generalized Gradient Approximation (GGA) using the Perdew-Burke-Ernzerhof (PBE) functional.[38,39] Long-range dispersion and van der Waals interactions were described through the Tkatchenko-Scheffler (TS) correction.[40] The Double Numerical plus Polarization (DNP) basis set was used for all atomic species to provide consistent accuracy in describing interatomic interactions carried out here.

The biotite surface model was created as a periodic 2 × 2 × 1 supercell including a 15 Å vacuum region perpendicular to the plane to eliminate spurious interactions between periodic images. Structural optimizations and electronic property calculations employed a Monkhorst-Pack **k**-point grid of 10 × 10 × 1 for the slab and only the Γ-point for isolated molecules. Convergence thresholds were set to 1×10^{-5} Ha for total energy, 1×10^{-6} Ha for the self-consistent field (SCF) cycle, and 5.0 Å for the orbital cutoff radius. A smearing of 0.005 Ha was applied to improve numerical stability during convergence.

Before complete DFT optimization of the structure of 2D biotite, the Adsorption Locator module implemented in the Materials Studio environment was employed to identify the most favorable adsorption sites of the molecules on the biotite surface. This procedure uses a global search algorithm that combines stochastic sampling with local relaxation, exploring various adsorption sites and orientations based on Lennard-Jones potentials and Universal Force Field interactions. The lowest-energy configurations obtained were subsequently refined within the same DFT framework described above to ensure structural and electronic consistency.

The stability of the molecule-surface interaction was quantified by the adsorption energy (E_{ads}), defined as (eq 1)

$$E_{ads} = E_{2D-Biotite/Molecules} - E_{2D-Biotite} - N_{molecule}\, E_{molecule} \quad (1)$$

where $E_{2D\text{-}Biotite/Molecules}$ is the total energy of the fully relaxed adsorbed system, $E_{2D\text{-}Biotite}$ is the total energy of the isolated biotite surface, $E_{molecule}$ is the energy of the isolated molecule, and $N_{molecule}$ is the number of adsorbed molecules. Negative values of E_{ads} indicate exothermic processes and energetically favorable adsorption. Charge transfer between the adsorbate and the substrate was evaluated using Hirshfeld charge analysis.[37] Negative values of Q_t indicate electron transfer from the surface to the molecule, while positive values indicate electron donation from the molecule to the substrate.

Electronic transport was studied by dividing a monolayer-based model system into three major parts: the left and right electrodes, which act as terminals for charge injection and collection, respectively, and the scattering region, which includes the biotite surface and the adsorbed molecules. Equilibrium geometries were determined from optimized adsorption structures obtained under various applied bias voltage conditions. *I*–*V* characteristics were calculated under the nonequilibrium Green's function (NEGF) formalism using a 25 × 1 × 1 k-point grid at a temperature of 300 K. This theoretical analysis establishes a direct connection between the charge redistribution caused by adsorption and the formation of new electronic transport pathways, which explains the observed current enhancement and frequency-dependent response in the system.

3. RESULT AND DISCUSSION

Figure 1a shows the XRD patterns of bulk and exfoliated 2D biotite samples. The diffraction peaks obtained at approximately 2θ = 19.6° (002), 26.7° (003), 36.4° (131), 47.6° (005), and 57.2° (204) correspond to the crystalline planes of biotite (crystallography open database reference code: 96-900-1267), confirming the preservation of its layered silicate structure even after exfoliation. Both spectra display the characteristic reflections of monoclinic biotite (C12/m1 space group),[22,30,38] although significant differences are observed in the relative intensities and sharpness of the peaks. The XRD peaks in bulk biotite appear sharp and high-intensity, confirming its high crystallinity and well-ordered layered stacking along the *c*-axis. After exfoliation, a decrease in the intensity of the (00 l) reflections (around 19.6° and 26.7°) and a broadening of the peaks are observed in 2D biotite. This change is due to fewer layers being stacked, a reduced crystallite thickness, and the strain generated during the delamination process. Furthermore, an increase in the FWHM of the (003) peak indicates a decrease in the coherent domain size along the *c*-axis, consistent with the formation of a few-layer structure.[25,33] The suppression of non-basal reflections such as (131), (005), and (204) in the XRD pattern indicates a partial reduction in long-range periodicity and misalignment of the exfoliated flakes. However, the clear presence of the (002) reflection confirms that exfoliation occurs primarily through interlayer separation, rather than complete disruption of the structure. The appearance of the (032) diffraction peak in the XRD pattern of 2D biotite is attributed to the structural reorientation and partial exfoliation of layered biotite during the

https://doi.org/10.1021/acsaelm.6c00747
ACS Appl. Electron. Mater. 2026, 8, 5750−5762

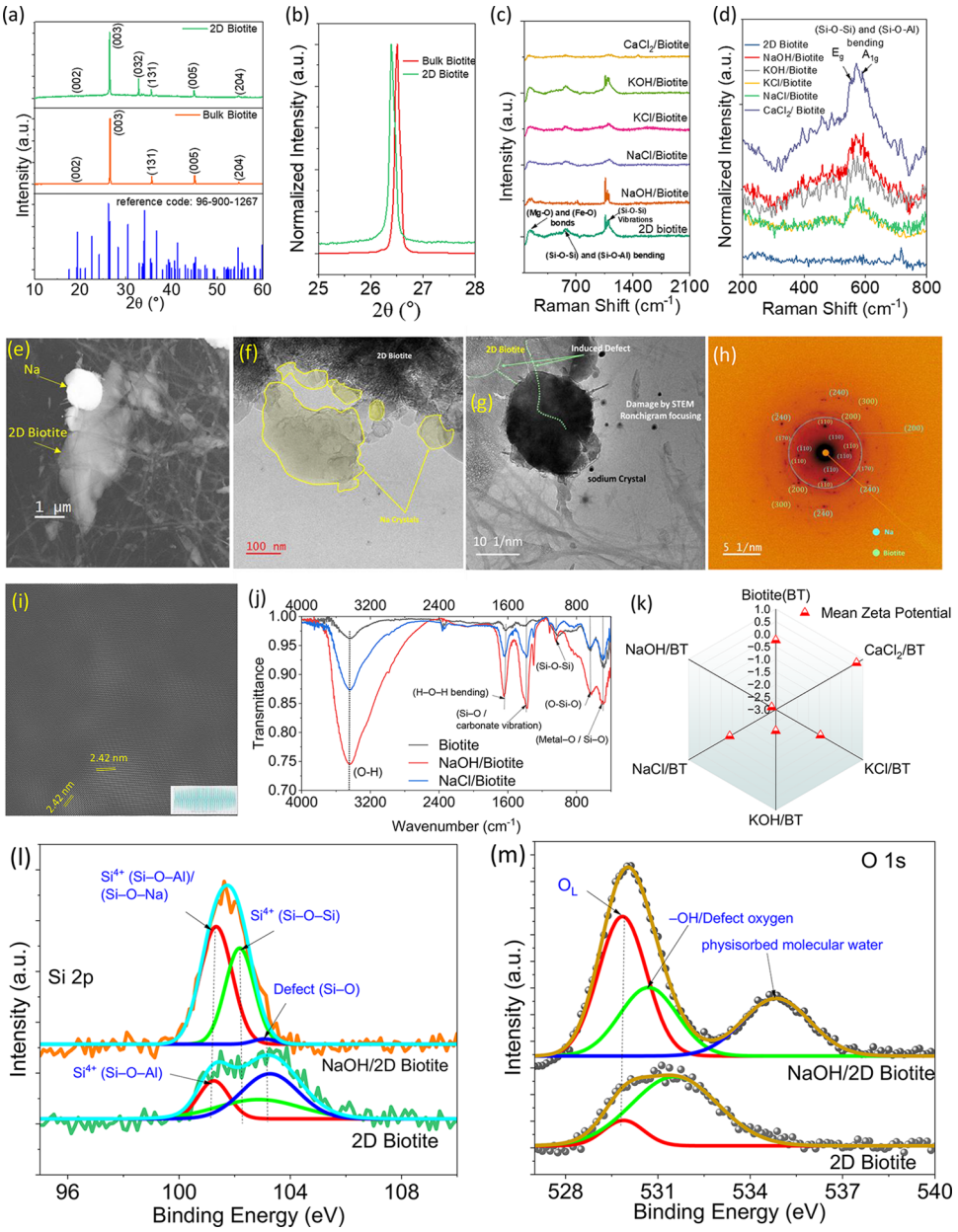

Figure 1. (a, b) XRD patterns of bulk and exfoliated 2D biotite. (c, d) Raman spectra showing vibrational modes corresponding to biotite and its functionalized states. (e, f) Transmission Electron Microscopy images reveal thin, wrinkled nanosheets with incorporated NaOH. (g) SAED pattern indicates a polycrystalline structure, while the High-Resolution Transmission Electron Microscopy image (h) shows a lattice spacing of 2.42 nm corresponding to the (002) plane of biotite. (i) High-resolution TEM (HRTEM) image of exfoliated 2D biotite nanosheets showing clear lattice fringes with an interplanar spacing of ∼2.42 nm, (j) Fourier Transform Infrared Spectroscopy spectrum illustrating the presence of functional groups and surface modifications. (k) The mean zeta potential of pristine biotite (BT) and biotite functionalized with different electrolytes (NaOH, NaCl, KOH, KCl, $CaCl_2$). XPS spectra of (l) Si 2p and (m) O 1 s for pristine 2D biotite and NaOH-treated 2D biotite.

synthesis process. The reduction in layer thickness and increased exposure of crystallographic planes can enhance the diffraction intensity of specific planes such as (032), which may remain weak or less distinguishable in bulk biotite. The slight shift of the (002)/(003) reflections towards a lower 2θ indicates a slight increase in interlayer spacing as a result of strain relaxation. The broadened and slightly shifted (003) peak (Figure 1b) indicates that the material has been successfully exfoliated into 2D nanosheets of a few-layer thickness while preserving the multilayer crystal structure.

The Raman analyses of pristine and functionalized 2D biotite are shown in Figure 1c. The pristine sample exhibits well-defined peaks corresponding to the vibrational modes of the silicate framework, observed in the range of 650–1100 cm^{-1}, associated with Si–O stretching and bending vibrations.[42,43] Upon functionalization with different electrolytes and alkalines, the relative intensities of existing peaks vary significantly. Modifications in the Raman response indicate slight changes in the vibrational modes, perhaps due to structural distortions and local charge redistribution within the biotite lattice, caused

https://doi.org/10.1021/acsaelm.6c00747
ACS Appl. Electron. Mater. 2026, 8, 5750−5762

by intercalation of ionic species and electrostatic interactions at the surfaces. Similar Raman shifts and broadening effects were observed for intercalated layered oxides, confirming that the functionalization alters the local bonding environment.[42,43] In Figure 1d, comparison of the Raman spectra obtained from pristine and functionalized devices is shown. The pristine biotite shows sharp peaks with high signal intensity, whereas the treated devices demonstrate a reduction in peak intensity and an increase in background scattering, suggesting enhanced electron–phonon coupling and localized defect states.[25,44] The strong suppression of characteristic modes indicates charge-transfer interactions between the biotite nanosheets and the ion species. The broadening of the Si–O and Mg/Fe–O vibrational modes reflects an increase in structural disorder,[45] which is consistent with the adsorption of electrolyte ions on the 2D surface. Raman mapping analyses (Supporting Information Figures S1–S6) clearly indicate the absence of any detectable impurity phases in all the synthesized samples.

The structural evolution of NaOH-functionalized 2D biotite was systematically investigated using TEM and HRTEM analyses (Figure 1e–i). After treatment with NaOH solution followed by drying, the TEM micrograph (Figure 1e) shows exfoliated and partially delaminated biotite sheets with Na-rich aggregates adhered to the surface, indicating successful Na incorporation and surface modification.[28] A HRTEM image (Figure 1f) reveals ultrathin biotite layers decorated with nanoscale Na-based crystallites, confirming an interlayer ion-exchange and nucleation process, where Na^+ ions diffuse into the silicate lattice and subsequently crystallize during the drying stage. High-magnification TEM (Figure 1g) shows ion-induced structural changes in the 2D biotite, including point defects, dislocations, and small amorphous regions. The image shows alkali-assisted exfoliation and subsequent lattice relaxation reported for NaOH-treated layered silicates. The SAED pattern (Figure 1h) displays distinct diffraction rings indexed to the biotite lattice and Na crystal phases, confirming the coexistence of crystalline biotite sheets and polycrystalline Na domains after functionalization. The lattice fringe analysis (Figure 1i) shows a measured d-spacing of ∼2.42 nm, indicating partial expansion of the biotite layers due to Na^+ intercalation while retaining long-range crystallinity.[46]

Figure 1j shows the FTIR spectra of pristine biotite, NaOH-treated biotite, and NaCl-treated biotite, which reveal significant changes in the surface functional groups and lattice structure after chemical treatment. The broad absorption band observed at $\sim cm^{-1}$ is attributed to O–H stretching vibrations of hydroxyl groups and adsorbed water molecules. The NaOH/Biotite sample exhibits a substantially enhanced O–H peak intensity, indicating increased surface hydroxylation and the formation of additional active sites after alkali treatment.[23,33,41] The absorption band near ∼1630 cm^{-1} corresponds to H–O–H bending vibrations of physically adsorbed water molecules. The strong peaks appearing in the cm^{-1} region are assigned to Si–O–Si asymmetric and symmetric stretching vibrations, confirming the preservation of the silicate framework of biotite after chemical modification. A noticeable variation in peak intensity and slight band shifting suggests structural distortion and interlayer modification induced by NaOH and NaCl treatment. The band observed around $\sim cm^{-1}$ is associated with Si–O or carbonate-related vibrations, indicating surface interaction and possible chemical activation of the layered structure. The weaker absorption bands in the cm^{-1} region correspond to O–Si–O bending vibrations, while the low-wavenumber peaks near cm^{-1} are attributed to Metal–O (Fe–O/Mg–O/Al–O) and Si–O bending vibrations originating from the octahedral and tetrahedral lattice sites of biotite.[23,33,41]

Figure 1k shows the average zeta potential of pure and electrolyte-modified biotite. Pure biotite (BT) exhibited a slightly positive potential (∼+0.5 mV). However, $CaCl_2$/BT exhibited a more positive potential due to the strong adsorption of divalent Ca^{2+} ions. These ions neutralize, and sometimes even overcompensate, the natural negative charges on the surface. NaCl/BT and KCl/BT exhibited moderately negative potentials (−1.5 to −2.0 mV), due to ion exchange between alkali metal cations and interlayer sites. The effect of K^+ was found to be slightly greater than that of Na^+. The most negative values (−2.5 to −3.0 mV) were observed in hydroxide-functionalized samples (NaOH/BT, KOH/BT), where the adsorption of OH^- and de-protonation of the surface increases the negative charge density. Zeta potential analysis confirms that the surface electrostatic properties of biotite can be effectively controlled by various ions.

Figure 1l,m shows a comparison of Si 2p and O 1 s core-level high-resolution XPS spectra for pure 2D biotite and NaOH-treated 2D biotite. Pure 2D biotite exhibits a prominent peak in the Si 2p region around 102.5–103.0 eV, indicating the presence of Si^{4+} in silicate networks, such as Si–O–Si and Si–O–Al tetrahedral linkages. This value is consistent with binding energy values reported in the literature for phyllosilicate and silicate glasses in this energy range.[47] The O 1 s spectrum of the pure sample shows a predominantly lattice oxygen contribution, while relatively weak components related to hydroxyl and adsorbed water are present in the higher energy region. This indicates a low density of surface defects and limited surface hydroxylation. This result is consistent with the generally accepted assignments of O 1 s peaks to network oxide oxygen, hydroxyl species, and molecular water in silicate materials.[48,49] Significant changes are visible in the spectrum after NaOH treatment. The intensity of defect-related and alkali-associated components (such as Si–O–Na/Si–O–Al regions) increases in the Si 2p spectrum, indicating incorporation of alkali ions, ion exchange with interlayer cations, and partial disruption of the tetrahedral network. This behavior is similar to the chemical shifts and defect formation observed after modification of aluminosilicate systems.[47] Additionally, the O 1 s spectrum of the NaOH-treated sample shows an increase in the intensity of high-binding-energy components, which are believed to be associated with hydroxyl/defect oxygen and physisorbed water. This reflects increased hydroxylation and the creation of new defect sites on the surface due to NaOH activation. Despite this, the prominent Si^{4+} peak remains in the Si 2p spectrum, confirming that the original silicate framework is largely preserved. The appearance of additional components and their increased intensity indicates increased surface disorder and chemical activation. Such deconvolution and assignment of multiple O 1 s components in oxide and silicate systems is well documented in XPS studies on glasses and silicates, where lattice oxygen, hydroxyl groups, and adsorbed water produce distinct peaks in similar binding energy regions.[48]

Figure 2a shows the fabrication steps of the 2D biotite-based flexible wearable sensor. A biotite suspension was drop-cast onto an IDE-patterned PET substrate and followed by a uniform sensing layer. The *I*–*V* curve obtained after NaOH treatment shows a significant increase in current compared to pure

https://doi.org/10.1021/acsaelm.6c00747
ACS Appl. Electron. Mater. 2026, 8, 5750−5762

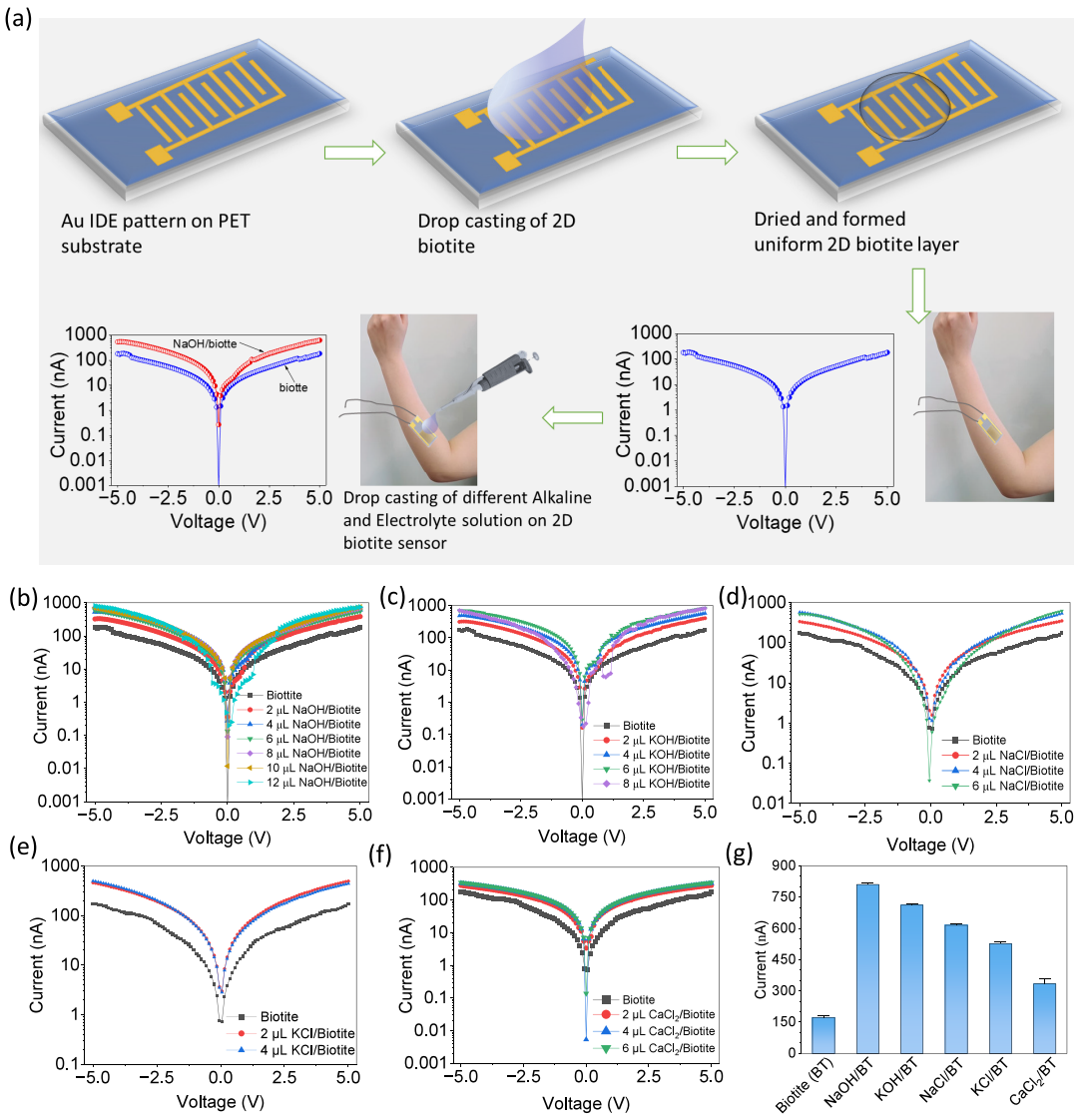

Figure 2. (a) Schematic representation of the fabrication steps, including drop-casting of 2D biotite on IDE-patterned PET substrate, followed by functionalization using various alkaline and electrolyte solutions, along with the corresponding *I–V* characteristics of pure and NaOH-functionalized biotite.*I–V* characteristics measurements of 2D biotite: (b) pristine and NaOH-functionalized, (c) KOH functionalized, (d) NaCl functionalized, (e) KCl-functionalized, and (f) $CaCl_2$ functionalized. (g) bar plot of current response for pristine biotite (BT) and electrolyte-functionalized biotite (NaOH/BT, KOH/BT, NaCl/BT, KCl/BT, $CaCl_2$/BT), showing enhanced current in functionalized samples compared to pristine BT.

biotite, indicating improved charge transport behavior as a result of alkaline functionalization. Furthermore, the sensor's easy adhesion to human skin demonstrates its high potential for use as a wearable sensing platform. Figure 2b–f show the *I–V* characteristics of 2D biotite after exposure to various ionic environments, specifically alkali hydroxides (NaOH, KOH), alkali halides (NaCl, KCl), and divalent metal halides ($CaCl_2$), to systematically assess the effect of ionic modification on its electrical conductivity. In all measurements, pristine 2D biotite exhibited the lowest current (~170 nA), reflecting its inherently low electrical conductivity. A remarkable increase in current was observed after functionalization, which can be attributed to increased carrier concentration and mobility through ion intercalation, surface hydroxylation, and defect engineering. The highest current increase was obtained in samples treated with NaOH and KOH. The concentration-dependent current increase with NaOH (2–12 μL) and KOH (2–8 μL) is a result of the combined effect of Na^+/K^+ intercalation, the formation of hydroxyl functional groups on the surface, and partial layer delamination.[1,14] Notably, in NaOH-treated biotite, the current reaches saturation at approximately 10 μL, indicating near-complete intercalation of interlayer active sites and surface doping. An increase in conductivity was also observed after NaCl and KCl functionalization, although this increase was relatively lower compared to hydroxide treatment. This trend was more pronounced at higher electric fields, where 6 μL of NaCl and 4 μL of KCl showed the best performance. This improvement is mainly due to additional carrier pathways arising from surface ion exchange and halide-induced defect formation. However, in the absence of hydroxyl-induced lattice activation, the overall conductivity enhancement remained limited. Divalent Ca^{2+} functionalization provided the most stable

https://doi.org/10.1021/acsaelm.6c00747
ACS Appl. Electron. Mater. 2026, 8, 5750−5762

and consistent improvement.[8] A nearly linear increase in current (ohmic behaviour) was observed with $CaCl_2$ (2–6 μL), with maximum conductivity recorded at 6 μL. This trend indicates improved structural density and strong electrostatic bonding of Ca^{2+} with the biotite lattice, confirming an extrinsic-doping-controlled ionic conduction mechanism. As shown in Figure 2g, all alkaline and electrolyte-functionalized 2D biotite sensors exhibited significant electrical performance of their optimized concentration NaOH (12 μL), KOH (8 μL), NaCl (6 μL), KCl (4 μL) and $CaCl_2$ (6 μL) compared to pristine 2D biotite, demonstrating that ion-controlled interfacial engineering is a powerful strategy for effectively controlling and optimizing the electrical characteristics of 2D biotite. This trend indicates an extrinsic doping–driven ionic conduction mechanism. The NaOH sensing performance of the 2D biotite device exhibited a strong linear relationship between current response and NaOH concentration, with a Pearson's correlation coefficient of 0.99081 and an adjusted R-square value of 0.9756, indicating excellent fitting accuracy. The linear fitting equation was obtained as ($y = 192.8 + 70.1x$), where the slope of 70.1 nA/μl represents the sensitivity of the sensor toward NaOH. Based on the calibration curve and using the standard (LOD = $3\sigma/S$) method, the estimated limit of detection (LOD) was calculated to be approximately 1.16 μl (Supporting Information Figure S7), demonstrating the capability of the sensor to detect low concentrations of NaOH with good sensitivity and reproducibility.

Figure 3a presents the impedance vs frequency spectra. Pristine 2D biotite shows a high magnitude at low frequencies with a steep decline as frequency increases, consistent with dielectric dispersion where charge carriers are localized (in traps, interlayer gaps, or across grain boundaries),[50,51] and only at higher frequencies can dipolar reorientation/interfacial polarization respond to the applied alternating field. Functionalization with electrolytes such as NaCl, KCl, NaOH, KOH, and $CaCl_2$ introduces mobile ionic species within or onto the surface of the biotite structure. These ions can adsorb onto surface defect sites, edges, or interlayer regions, increasing effective ionic conductivity and enabling space-charge screening. Consequently, a reduction in total impedance is observed across the entire frequency spectrum. NaOH and KOH treatments exhibit the greatest impedance reduction in functionalized samples. This is due to the small size, high mobility, and strong ability of OH^- ions to effectively polarize and screen electric fields at the surface/interface. This behavior is similar to results observed in semiconducting oxides and mixed ionic-electronic conductors, where additional ionic species reduce charge transfer resistance and interfacial polarization impedance. For example, impedance analysis of hematite electrodes modified with cobalt-phosphate catalysts shows that the addition of surface coating layers or electrolyte-based treatments alters both the resistive and capacitive components, resulting in a decrease in interfacial recombination and an increase in capacitive coupling.[52] Figure 3b shows the relative impedance response ($\Delta Z/Z\%$) of pure biotite (BT) and BT samples treated with various salts, which exhibits a strong dependence on the type of ionic species involved. NaCl/BT and $CaCl_2$/BT exhibit a clear increase in impedance with increasing frequency, indicating increased ion-lattice coupling and polarization effects at the biotite interface. In contrast, KCl/BT exhibits only a slight increase, while alkaline-treated samples (NaOH/BT and KOH/BT) remain virtually unchanged across the entire frequency range. This indicates limited ionic interactions or charge trapping within the layered structure. Pure biotite exhibits moderate changes with frequency, confirming its fundamental dielectric behavior.

Figure 4a shows a schematic diagram of the 2D biotite-based TENG and its measurement setup. During mechanical vibration, the Kapton and biotite layers repeatedly contact and separate, causing electrons to transfer from the Kapton to the 2D biotite due to the difference in their triboelectric polarities. The potential difference generated at the time of separation induces a flow of electrons through an external circuit,

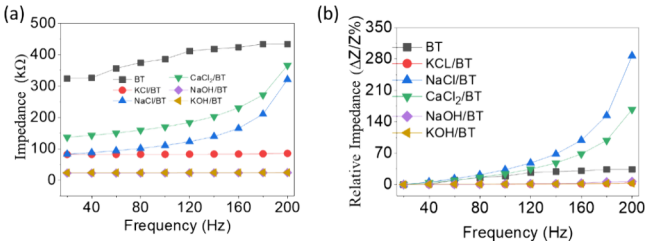

Figure 3. (a) Frequency-dependent impedance spectra of pristine 2D biotite (BT) and functionalized BT: BT, NaOH/BT, KOH/BT, NaCl/BT, KCl/BT, and $CaCl_2$/BT. (b) Relative impedance change of pristine biotite (BT) and treated biotite samples (KCl/BT, NaCl/BT, CaCl2/BT, NaOH/BT, and KOH/BT) as a function of frequency.

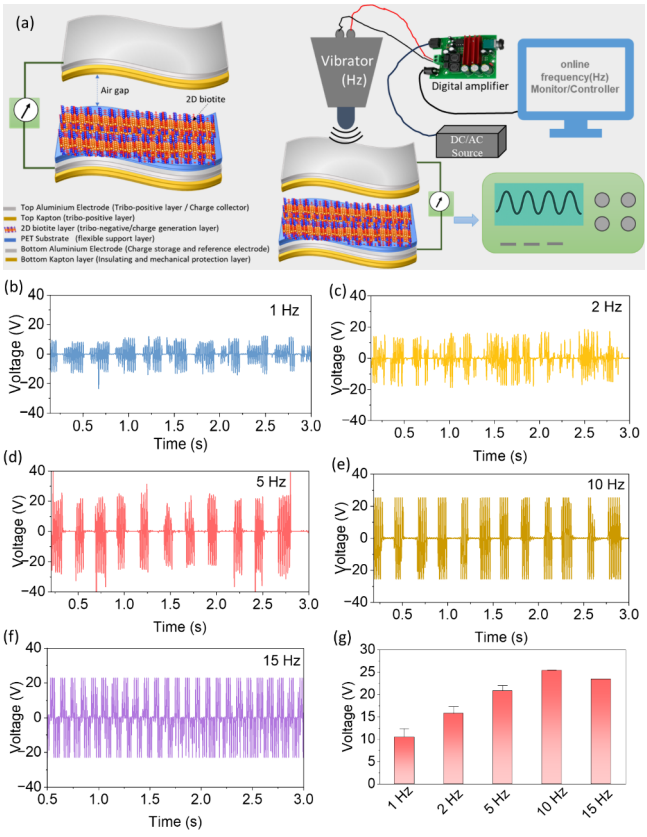

Figure 4. (a) Schematic illustration of the 2D biotite-based triboelectric nanogenerator coupled with a vibration-driven setup, controlled by an online frequency monitor, enabling real-time output measurements. (b–f) Output voltage–time signals of the TENG at different excitation frequencies of 1, 2, 5, 10, and 15 Hz are shown. (g) Peak output voltages obtained at different excitation frequencies.

https://doi.org/10.1021/acsaelm.6c00747
ACS Appl. Electron. Mater. 2026, 8, 5750–5762

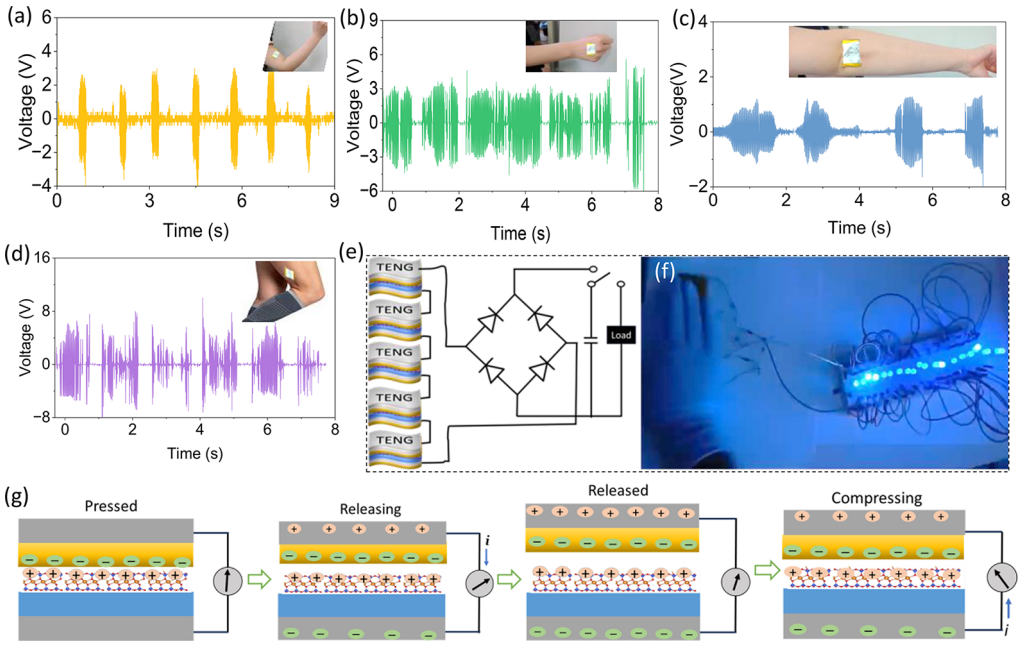

Figure 5. Output voltage responses of the 2D biotite-based flexible triboelectric nanogenerator attached to the under different body part opening and -closing motions: (a) biceps movement (3–4 V), (b) hand movements (1–1.5 V), (c) near elbow (3–3.5 V), (d) back thigh (4–6 V). (e, f) Demonstration of the flexible TENG device powering multiple blue LEDs upon mechanical pressing. (g) Sequential working stages of the TENG: contact generates triboelectric charges at the interface, separation, and layers approaching again; current and electron flow directions are shown.

generating an alternating voltage through the triboelectric effect and electrostatic induction.[53] The output performance (Figure 4b–f) shows that the voltage increases with increasing frequency from 1 to 10 Hz, due to an increase in the number of contact-separation cycles and improved charge transfer. A slight decrease in voltage is observed at 15 Hz because the extremely intense vibration reduces the effective contact time, preventing complete charge transfer. The summary graph (Figure 4g) shows a nearly linear increase in peak voltage up to 10 Hz and a slight decline thereafter. This device is effective in low-frequency energy harvesting, with its best performance achieved around 10 Hz. The current density and power density increased progressively with increasing operating frequency from 1 to 10 Hz, indicating enhanced triboelectric charge generation and improved interfacial charge transfer during repeated contact–separation cycles. As shown in Supporting Information Figure S8a, the current density increased from approximately 5.76 μA/cm^2 at 1 Hz to a maximum value of ∼16.9 μA/cm^2 at 10 Hz. Similarly, the power density shown in Figure S8b increased steadily and reached a maximum value of ∼0.373 mW/cm^2 at 10 Hz. The improved electrical performance is mainly attributed to the increased rate of periodic contact and separation, which promotes higher surface charge accumulation and accelerates electron transport kinetics within the layered biotite structure.

Figure S9a–f shows a comparison of the output voltages of pure and surface-modified biotite-based TENGs at 10 Hz. The pure device exhibits a stable amplitude of approximately ±24.3 V, while functionalization with $CaCl_2$, NaCl, KCl, NaOH, and KOH results in a slight decrease in the output voltage amplitude, as well as an upward shift in the baseline potential. This change reflects the increased built-in potential and interfacial polarization caused by the modification of the surface charge density by ionic and hydroxyl species. The reduced voltage output is attributed to charge screening and defect-mediated leakage, whereas increased surface conductivity enhances current generation.

The wearable TENG's response was dependent on the location of the body parts where they were mounted.[54] The location-dependent output performance measured is presented in Figure 5a–d. Attaching the device to the biceps produced ∼3–4 V, driven by significant muscle contraction and effective contact–separation. Whereas, near the elbow, a limitation in the spatial span caused by bending the elbow resulted in a reduced output of ∼1–1.5 V. Opening and closing of the palm generated well-defined pulses of 3–3.5 V, due to consistent motion and interfacial contact. The highest voltage of 4–6 V was recorded when the TENGs were located near the back thigh (hamstring region) due to greater mechanical deformation and a larger contact area during leg movement. Figure 5e shows a practical demonstration of the biotite-based TENG's capability to provide operational energy to simple devices. The TENG's were connected to a bridge rectifier circuit and an LED array on a breadboard. In the idle state, where the TENGs were not subjected to any kind of pressure and/or impulse (no significant light emission was observed from the LEDs), confirming the absence of electrical output. Upon mechanical tapping on the TENG (Figure 5f), the generated alternating triboelectric potential was effectively rectified and stored, leading to the illumination of multiple LEDs. Movie S1–V4 related to Figure 5 demonstrates the real-time operation and performance of the developed device under different working conditions. This setup highlights the self-powered and rectified energy-harvesting capability of the TENG, establishing its potential for use in the future for wearable smart sensing systems.

https://doi.org/10.1021/acsaelm.6c00747
ACS Appl. Electron. Mater. 2026, 8, 5750−5762

4. SENSING MECHANISM

The combined *I*–*V*, impedance–frequency, and triboelectric measurements consistently point to a mechanism in which ion adsorption, interlayer exchange, and surface chemical modification regulate electrical transport and the contact-electrification behavior of 2D biotite films. Across the concentration series, conductivity increases monotonically with analyte loading (Figure 2c–g), with monovalent salts and alkaline treatments (NaCl, KCl, NaOH, KOH) producing enhancement in current and the strongest suppression of low-frequency impedance (Figure 3a,b). This behavior is consistent with an increase in the total charge conductivity (eq 2):

$$\sigma_{tot} = n_e e\mu_e + \Sigma_i n_i z_i e\mu_i \quad (2)$$

It is driven primarily by a higher density of mobile ionic carriers (n_i) and/or enhanced carrier mobility (μ_i) arising from facile cation exchange (BT–K^+ ↔ BT–M^+) and surface deprotonation (–OH formation) induced by OH^-.[24,55] In the layered structure of biotite, K^+ ions serve as the native interlayer cations, stabilizing the negatively charged silicate sheets. Upon exposure to electrolyte solutions, these interlayer K^+ ions can undergo partial exchange with external substituting monovalent cations (M^+, e.g., Na^+, K^+ from the electrolyte). $CaCl_2$ yields comparatively smaller increases in DC, despite often producing significant surface charge modulation. This can be explained by the stronger binding or cross-linking of Ca^{2+} to silicate oxygens, which enhances surface charge but reduces ionic mobility (μ_i), in agreement with prior reports on limited interlayer exchange of divalent species in micas.[25] In addition, drying can lead to partially immobilized interfacial layers or insoluble complexes, thereby limiting the ionic contribution to conductivity (σ_{ion}).[56]

The operating mechanism of the TENG is governed by the coupling of contact electrification and electrostatic induction processes.[53] Generation of open-circuit voltage (V_{oc}) and short-circuit current (I_{sc}) during the periodic contact–separation cycles.[57,58] At the original state, no surface charge or induced potential difference (EPD) exists between the two Al electrodes.[59] Both layers, Kapton (tribo-negative) and 2D biotite (tribo-positive), are electrically neutral ($V_{OC} = 0$). Upon mechanical contact (Figure 5g), surface charge transfer occurs at the interface due to the triboelectric effect. According to the triboelectric series, 2D biotite, being more electropositive, loses electrons, while Kapton gains electrons, resulting in net positive charges (+σ) on the 2D biotite surface and negative charges (–σ) on the Kapton surface. The insulating properties of both materials allow these triboelectric charges to be stably retained for extended durations. Since the charges are confined to atomically thin surface regions, opposite charges coincide in nearly the same plane, leading to a negligible electrostatic potential difference immediately after contact. As the external force is released, the elastic recovery of the Kapton film and PET substrate initiates separation between the triboelectric layers. This charge separation creates an electrostatic potential difference (EPD) between the electrodes, which drives the flow of electrons from the lower (biotite) electrode to the upper (Kapton) electrode through the external circuit. As a result, a positive open-circuit voltage (V_{oc}) is recorded at the upper electrode, which increases as the distance between the layers increases. The induced potential difference can be expressed as (eq 3):

$$V_{oc} = \frac{\sigma d}{\varepsilon_0} \quad (3)$$

where (σ) is the triboelectric surface charge density, ε_0 is the vacuum permittivity, and d is the instantaneous separation distance between the two charged surfaces.[53]

At the point of maximum displacement, charge equilibrium is established between the electrodes, resulting in saturation of V_{oc}. During the subsequent contact phase, the electrostatic field intensity decreases as the separation distance (d') gradually decreases. This results in a decrease in the EPD and a re-flow of electrons toward the lower electrode, manifesting as a reverse ISC. When the two layers are back in close contact, there is no further charge redistribution, and the EPD ends, completing a complete cycle.[58]

5. THEORETICAL RESULTS AND DISCUSSION

First-principles calculations were performed to understand the adsorption processes and electronic transport mechanisms occurring on two-dimensional biotite surfaces at the atomic level. The primary objective of this study was to elucidate how small ionic particles interact with the silicate substrate and affect its electronic properties and conductivity. To this end, NaCl, KCl, $CaCl_2$, NaOH, and KOH systems were selected based on their different dissociation properties and polarity, allowing a comparative analysis of how these factors control interfacial coupling and the overall electrochemical reactivity of the material. The simulated device structure (Figure 6a) used in the transport calculations consists of a biotite monolayer connected to left and right metallic electrodes, which together define the scattering region. The current–voltage curves shown in Figure 6b and the current intensity at 5 V in Figure 6c indicate that the theoretical results accurately reproduce the experimental trend. The order obtained is BT/NaOH > BT/KOH > BT/NaCl > BT/KCl > BT/$CaCl_2$ > BT, which is consistent with the experimental results. Comparing the current magnitudes, it is clear that the adsorption of hydroxide ions produces the largest increase in current. This agreement between theoretical and experimental results indicates that the change in conductivity is primarily related to the stability of the adsorbed species on the biotite surface. To understand the microscopic origin of this trend, optimized adsorption geometries (Figure 6d–h), presented in top and side views, provide important insights. The BT/NaOH and BT/KOH systems exhibit the highest adsorption energies of –2.79 and –2.05 eV, respectively, indicating strong chemical anchoring with the substrate. This stable interaction promotes local bond formation and charge reorganization, thereby reducing interfacial barriers and facilitating electronic transport. Consequently, higher currents are observed in these systems, indicating that adsorption energy is the primary factor controlling the electrochemical reaction, while charge transfer plays a secondary role. The slightly higher current is observed in BT/NaOH than in BT/KOH, which can be explained by the relatively higher charge transfer in the KOH system. Thus, the combined effect of adsorption energy and charge redistribution governs electronic transport and overall electrochemical behavior in 2D biotite systems.

In the BT/NaCl system, as shown in Figure 6f, the adsorption energy is moderate (–0.94 eV) and charge transfer is very

https://doi.org/10.1021/acsaelm.6c00747
ACS Appl. Electron. Mater. 2026, 8, 5750–5762

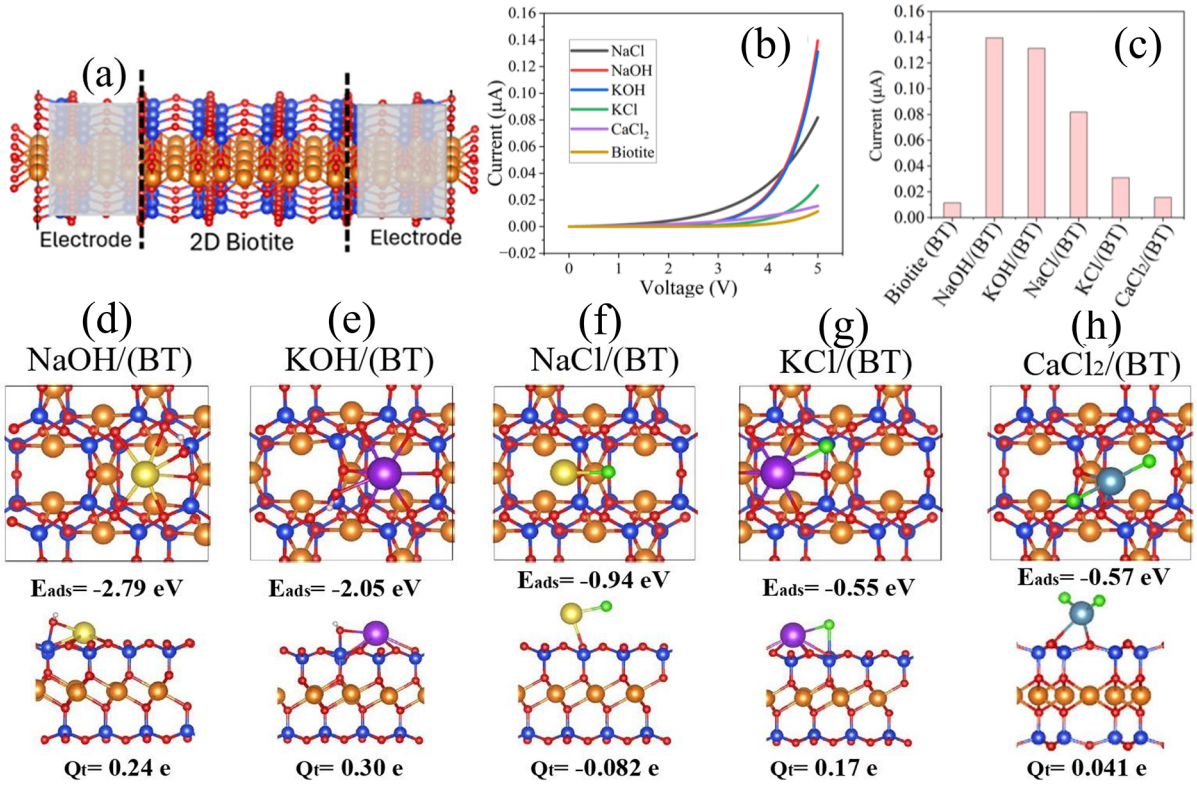

Figure 6. (a) Schematic representation of the simulated device, composed of a 2D biotite layer connected to left and right electrodes. (b) Calculated *I-V* curves for pristine biotite and for systems with adsorbed ionic species (NaCl, NaOH, KOH, KCl, and $CaCl_2$). (c) Comparison of the current values at 5 V for each configuration. Optimized adsorption configurations of ionic species on the biotite surface: (d) NaOH, (e) KOH, (f) NaCl, (g) KCl, and (h) $CaCl_2$. Top and side views are shown for each system. The corresponding adsorption energies (E_{ads}) and net charge transfers (Q_t) indicate distinct adsorption strengths and charge redistribution behaviors depending on the adsorbed molecule.

low, placing this system in the middle position in the current hierarchy. The BT/KCl and BT/$CaCl_2$ systems, shown in Figure 6g,h, exhibit similar adsorption energies of –0.55 and –0.57 eV, respectively. Although $CaCl_2$ has a slightly lower adsorption energy, its current remains lower than that of BT/KCl. This difference arises primarily due to lower charge transfer and partial immobilization of Ca^{2+} ions at the interface, which limits charge mobility and reduces conductivity. The results indicate that the strength of adsorption and the electrochemical response determine the general ordering between different systems. When adsorption energies are approximately equal, charge transfer acts as a secondary factor, further explaining the difference between them. This combination of effects is consistent with the experimental trend, where stronger adsorption and more effective charge redistribution lead to higher currents and better interfacial coupling. Therefore, ion–silicate interactions play a key role in controlling the conductivity and overall electrical behavior in 2D biotite systems.

This study introduces a novel concept of material-synchronized self-powered ion sensing, in which a single natural 2D material simultaneously performs ion recognition, signal transduction, and energy harvesting. By demonstrating that ion adsorption and triboelectric charge generation can be naturally interconnected within 2D biotite, rather than being artificially engineered through multi-material-based hybrid architectures, this work redefines how autonomous sensing systems can be designed. This conceptual change thus advances self-powered sensors beyond mere device-level integration and toward material-level multifunctionality. Additionally, it demonstrates that electro-ionic and triboelectric phenomena in natural layered minerals may be deeply intertwined, paving the way for a new and yet unexplored material field for sustainable, battery-free nanotechnologies.

6. CONCLUSION

This work presents 2D biotite as a previously under-explored but highly attractive multifunctional material that combines ion-responsive electronics with self-powered energy harvesting—a key requirement for next-generation wearable electronics. Targeted alkaline and electrolyte treatments optimized the interlayer distance, surface chemistry, and defect states, strengthening ion adsorption and significantly improving the transport of charge carriers across the 2D biotite interface. Electrical conductivity increased by >4.5× (from ∼170 to ∼800 nA for NaOH treatment), along with a reduction in impedance and minimization of polarization losses, clearly establishing the ion–electron coupling mechanism. The flexible 2D biotite-based TENG provided a maximum output of ±10.34 to ±24.3 V at 1–10 Hz and stored energy from 1 to 6 V from real human motions, enabling the operation of flash LEDs and confirming battery-free operation. The DFT and NEGF simulations supported the experimental observations by showing favorable ion adsorption energetics and the formation of efficient charge-transfer pathways that regulate ion-driven conductivity modulation.

https://doi.org/10.1021/acsaelm.6c00747
ACS Appl. Electron. Mater. 2026, 8, 5750–5762

Collectively, the findings highlight 2D biotite as a sustainable and scalable dual-purpose material for self-powered ion sensing in wearable applications.

■ ASSOCIATED CONTENT

Supporting Information

The Supporting Information is available free of charge at https://pubs.acs.org/doi/10.1021/acsaelm.6c00747.

Raman mapping of sensing samples; limit of detection of the NaOH/biotite sensor; current density and power density of the 2D biotite TENG device; voltage–time responses of the pristine and surface-functionalized NaOH-, KOH-, NaCl-, KCl-, and $CaCl_2$-functionalized 2D biotite TENGs at 10 Hz (DOCX)

Real-time device performance under dynamic arm movements (MP4)

Voltage generation during repetitive elbow flexion–extension movements (MP4)

Voltage generation during hand-grip motions (MP4)

LED flashing induced by hand-tapping motions (MP4)

■ AUTHOR INFORMATION

Corresponding Authors

Douglas S. Galvão – *Department of Applied Physics and Center for Computational Engineering and Sciences, State University of Campinas, Campinas 13083-859, São Paulo, Brazil;* orcid.org/0000-0003-0145-8358; Email: galvao@ifi.unicamp.br

Chandra Sekhar Tiwary – *Department of Metallurgical and Materials Engineering, Indian Institute of Technology Kharagpur, Kharagpur 721302, India;* orcid.org/0000-0001-9760-9768; Email: chandra.tiwary@metal.iitkgp.ac.in

Authors

Sumit Kumar – *Department of Metallurgical and Materials Engineering, Indian Institute of Technology Kharagpur, Kharagpur 721302, India;* orcid.org/0000-0001-8898-2448

Kleuton A. L. Lima – *Department of Applied Physics and Center for Computational Engineering and Sciences, State University of Campinas, Campinas 13083-859, São Paulo, Brazil;* orcid.org/0000-0003-4699-5886

Raphael M. Tromer – *Institute of Physics, University of Brasília, Brasília, DF 70919-970, Brazil;* orcid.org/0000-0002-6180-5641

Dipanwita Mitra – *Department of Physics, Indian Institute of Technology Kharagpur, Kharagpur 721302, India*

Saswata Goswami – *Department of Physics, Indian Institute of Technology Kharagpur, Kharagpur 721302, India*

Surbhi Slathia – *School of Nano Science and Technology, Indian Institute of Technology Kharagpur, Kharagpur 721302, India*

Marcelo L. Pereira Junior – *#Department of Materials Science and NanoEngineering, Rice University, Houston, Texas 77005, United States; Department of Electrical Engineering, College of Technology, University of Brasília, Brasília 70910-900, Federal District, Brazil;* orcid.org/0000-0001-9058-510X

Michael E. McConney – *Materials and Manufacturing Directorate, Air Force Research Laboratory, Wright-Patterson Air Force Base, Ohio 45433, United States*

Ajit K. Roy – *Materials and Manufacturing Directorate, Air Force Research Laboratory, Wright-Patterson Air Force Base, Ohio 45433, United States;* orcid.org/0000-0002-3344-7437

Saikat Talapatra – *Department of Metallurgical and Materials Engineering, Indian Institute of Technology Kharagpur, Kharagpur 721302, India; School of Physics and Applied Physics, Southern Illinois University Carbondale, Carbondale, Illinois 62901, United States*

Mauricio Terrones – *Department of Physics and Materials Research Institute, The Pennsylvania State University, University Park, Pennsylvania 16802, United States;* orcid.org/0000-0003-0010-2851

Complete contact information is available at: https://pubs.acs.org/doi/10.1021/acsaelm.6c00747

Author Contributions

#S.K. and K.A.L.L. contributed equally to this work. S.K.: Investigation, Conceptualization, Methodology, Data curation, Formal analysis, Validation, Writing—original draft. K.A.L.L.: DFT Software, Data curation, Formal analysis, Writing—review and editing. R.M.T.: Software, Writing—review and editing. D.M.: Formal analysis, Writing—review and editing. S.G.: Formal analysis, Writing—review and editing. S.S.: Formal analysis, Writing—review and editing. M.L.P.J.: Simulation Software, Writing—review and editing. M.E.M.: Formal analysis, Writing—review and editing. A.K.R.: Formal analysis, Writing—review and editing. S.T.: Formal analysis, Writing—review and editing. M.T.: Formal analysis, Writing—review and editing. D.S.G.: Supervision, Resources, Validation, Writing—review and editing. C.S.T.: Conceptualization, Writing—review and editing, Visualization, Funding acquisition, Validation, Supervision, Resources, Project administration.

Notes

The authors declare no competing financial interest.

■ ACKNOWLEDGMENTS

C.S.T. acknowledges AOARD (Asian Office of Aerospace Research and Development) grant no. FA2386–21–1–4014, and Naval Research Board for funding support. C.S.T. acknowledges the funding support of AMT and Energy & Water Technologies of TMD Division of DST. The author acknowledges RISING Center at Rice University for support.

■ REFERENCES

(1) Wang, F.; Liu, Y.; Zhang, M.; Zhang, F.; He, P. Home Detection Technique for Na+ and K+ in Urine Using a Self-Calibrated All-Solid-State Ion-Selective Electrode Array Based on Polystyrene-Au Ion-Sensing Nanocomposites. *Anal. Chem.* **2021**, *93* (23), 8318–8325.

(2) Ikhsan, M. M.; Yang, C.; Ghotia, K.; Egert, F.; Ansar, S. A.; Żurowska, O.; Rózga, M.; Michalak, A.; Kraglund, M. R.; Aili, D.; Park, H. S.; Razmjooei, F.; Henkensmeier, D. Sulfonated Polybenzimidazole for Low-Alkalinity Ion Solvating Membrane Water Electrolysis. *Nat. Energy* **2025**, *10* (11), 1347–1359.

(3) KavyaDeepu, R. M.; Sekar, M. A Comprehensive Review of Electrolyte Imbalances and Their Applied Aspects in Dermatology. *Cureus* **2025**, *17*, e81353.

(4) Bandodkar, A. J.; Jeerapan, I.; Wang, J. Wearable Chemical Sensors: Present Challenges and Future Prospects. *ACS Sens.* **2016**, *1* (5), 464–482.
(5) Possanzini, L.; Decataldo, F.; Mariani, F.; Gualandi, I.; Tessarolo, M.; Scavetta, E.; Fraboni, B. Textile Sensors Platform for the Selective and Simultaneous Detection of Chloride Ion and PH in Sweat. *Sci. Rep.* **2020**, *10* (1), 17180.
(6) Modisett, A. K.; Patel, R. M.; Jernigan, S. M.; Figueroa, J.; Sewell, E. K.; Hamrick, S. E. G. Patterns of Acute Kidney and Hepatic Injury and Association with Adverse Outcomes in Infants Undergoing Therapeutic Hypothermia for Hypoxic Ischemic Encephalopathy. *J. Perinatol.* **2022**, *42* (10), 1361–1367.
(7) Phillips, D. R.; Ahmad, K. I.; Waller, S. J.; Meisner, P.; Karet, F. E. A Serum Potassium Level above 10 Mmol/l in a Patient Predisposed to Hypokalemia. *Nat. Clin. Pract. Nephrol.* **2006**, *2*, 340–346.
(8) Brown, E. M. Clinical Lessons from the Calcium-Sensing Receptor. *Nat. Rev. Endocrinol.* **2007**, *3*, 122–133.
(9) Shah, A. H.; Zhang, Z.; Huang, Z.; Wang, S.; Zhong, G.; Wan, C.; Alexandrova, A. N.; Huang, Y.; Duan, X. The Role of Alkali Metal Cations and Platinum-Surface Hydroxyl in the Alkaline Hydrogen Evolution Reaction. *Nat. Catal.* **2022**, *5* (10), 923–933.
(10) Hu, J.; Tang, X.; Dai, Q.; Liu, Z.; Zhang, H.; Zheng, A.; Yuan, Z.; Li, X. Layered Double Hydroxide Membrane with High Hydroxide Conductivity and Ion Selectivity for Energy Storage Device. *Nat. Commun.* **2021**, *12* (1), 3409.
(11) Sanjay, S.; Hossain, M.; Rao, A.; Bhat, N. Super-Nernstian Ion Sensitive Field-Effect Transistor Exploiting Charge Screening in WSe2/MoS2 Heterostructure. *npj 2D Mater. Appl.* **2021**, *5* (1), 93.
(12) Ma, W.; Sun, Y.; Wang, C.; Wang, P. Mutual Promotion of Triboelectric Nanogenerators and Field-Effect Transistors towards the IoT. *Nat. Rev. Electron. Eng.* **2025**, *2* (8), 541–554.
(13) Shao, Y.; Ying, Y.; Ping, J. Recent Advances in Solid-Contact Ion-Selective Electrodes: Functional Materials, Transduction Mechanisms, and Development Trends. *Chem. Soc. Rev.* **2020**, *49*, 4405–4465.
(14) Kim, D. Y.; Reza, M. S.; Samad, A. A.; Islam, Z.; Go, J. W.; Park, J. Y. A Highly Stable and Flexible Ion-Selective Patch Sensor for Real-Time Sweat Na+ and K+ Monitoring. *Micro and Nano Syst. Lett.* **2025**, *13*, 15.
(15) Fakih, I.; Durnan, O.; Mahvash, F.; Napal, I.; Centeno, A.; Zurutuza, A.; Yargeau, V.; Szkopek, T. Selective Ion Sensing with High Resolution Large Area Graphene Field Effect Transistor Arrays. *Nat. Commun.* **2020**, *11* (1), 3226.
(16) Nguyen, T. T. H.; Nguyen, C. M.; Huynh, M. A.; Vu, H. H.; Nguyen, T. K.; Nguyen, N. T. Field Effect Transistor Based Wearable Biosensors for Healthcare Monitoring. *J. Nanobiotechnol.* **2023**, *21*, 411.
(17) Lv, J.; Wang, J.; Yang, L.; Liu, W.; Fu, H.; Chu, P. K.; Liu, C. Recent Advances of Optical Fiber Biosensors Based on Surface Plasmon Resonance: Sensing Principles, Structures, and Prospects. *Sens. Diagn.* **2024**, *3*, 1369–1391.
(18) Cho, S.; Shajari, S.; Xiong, Y.; Madsen, K.; Lv, Z.; Cho, S.; Park, J.; Li, M.; Li, S.; Feng, L.; Song, R.; Şahin, S.; Huang, I.; Nuxoll, R. F.; Zhou, Y.; Kang, Y.; Park, C.; Park, J.; Huang, Y.-T.; Wapnick, S.; Bukaric, H.; Mueller, X.; Opal, S.; Chen, Z.; Taechamahaphan, A.; Aranyosi, A. J.; Park, K.-C.; Ghaffari, R.; Lee, H.; Huang, Y.; Oh, S.; Rogers, J. A. Wearable Lateral Flow Assays for Cortisol Monitoring with Time-Dynamic Sweat Sampling and Sensing by Electrochromic Timers. *Nat. Sens.* **2026**, *1* (1), 85–98.
(19) Pan, L.; Zhou, D.; Wang, Y. Recent Advances in Biosensors Based on the Electrochemical Properties of MXenes. *Analyst* **2025**, *150*, 2469–2488.
(20) Kaja, K. R.; Hajra, S.; Pharino, U.; Bhosale, P. S.; Panda, S.; Belal, M. A.; Sriphan, S.; Khanapuram, U. K.; Vittayakorn, N.; Kim, H. J. High-Performance Droplet-Driven Electrification for Self-Powered Real-Time Nitrate Monitoring in Agricultural Water Systems. *J. Sci.: Adv. Mater. Dev.* **2026**, *11* (2), 101154.
(21) Hajra, S.; Panda, S.; Kaja, K. R.; Belal, M. A.; Vivekananthan, V.; Kim, H. J. Self-Powered Fire Safety Indicator Based on Fabric-Based Triboelectric Nanogenerator. *Energy Technol.* **2025**, *13* (10), 240288.
(22) Hajra, S.; Kaja, K. R.; Panda, S.; Song, S.; Jeong, S. M.; Mishra, Y. K.; Oh, T. H.; Das, G.; Divya, S.; Kim, H. J. Mechanoluminescence: Mechanisms, Emerging Applications, and Future Prospects. *Nano Energy* **2025**, *145*, 111418.
(23) Mitra, D.; Hasan, M. N.; Gowda, C. C.; Costin, G.; Tiwary, C. S.; Karmakar, D.; Datta, P. K. Vacancy-Enhanced Biotite Nanosheets for Optical Limiters. *ACS Appl. Nano Mater.* **2025**, *8*, 8187.
(24) Meunier, M.; Currie, J. F.; Wertheimer, M. R.; Yelon, A. Electrical Conduction in Biotite Micas. *J. Appl. Phys.* **1983**, *54* (2), 898–905.
(25) Mahapatra, P. L.; Tromer, R.; Pandey, P.; Costin, G.; Lahiri, B.; Chattopadhyay, K.; Ajayan, P. M.; Roy, A. K.; Galvao, D. S.; Kumbhakar, P.; Tiwary, C. S. Synthesis and Characterization of Biotene: A New 2D Natural Oxide From Biotite. *Small* **2022**, *18* (27), 2201667.
(26) Franceschi, G.; Kocán, P.; Conti, A.; Brandstetter, S.; Balajka, J.; Sokolović, I.; Valtiner, M.; Mittendorfer, F.; Schmid, M.; Setvín, M.; Diebold, U. Resolving the Intrinsic Short-Range Ordering of K+ Ions on Cleaved Muscovite Mica. *Nat. Commun.* **2023**, *14* (1), 208.
(27) Park, T.; Lee, C. H. Wearables That Learn to Read Gestures on the Move. *Nat. Sens.* **2026**, *1* (1), 12–13.
(28) Zou, Y. C.; Mogg, L.; Clark, N.; Bacaksiz, C.; Milovanovic, S.; Sreepal, V.; Hao, G. P.; Wang, Y. C.; Hopkinson, D. G.; Gorbachev, R.; Shaw, S.; Novoselov, K. S.; Raveendran-Nair, R.; Peeters, F. M.; Lozada-Hidalgo, M.; Haigh, S. J. Ion Exchange in Atomically Thin Clays and Micas. *Nat. Mater.* **2021**, *20* (12), 1677–1682.
(29) Oliveira, R., de; Barbosa Yoshida, A. B.; Rabahi, C. R.; O Freitas, R.; Teixeira, V. C.; Matos, C. J. S., de; Galvão Gobato, Y.; Barcelos, I. D.; Cadore, A. R. Ultrathin Natural Biotite Crystals as a Dielectric Layer for van Der Waals Heterostructure Applications. *Nanotechnology* **2024**, *35* (50), 505703.
(30) Pérez-Maqueda, L. A.; Blanes, J. M.; Pascual, J.; Pérez-Rodríguez, J. L. The Influence of Sonication on the Thermal Behavior of Muscovite and Biotite. *J. Eur. Ceram. Soc.* **2004**, *24* (9), 2793–2801.
(31) Khan, M. Z.; Vervelaki, A.; Jetter, D.; Bagani, K.; Ney, A.; Peil, O. E.; Valencia, S.; Smekhova, A.; Kronast, F.; Knez, D.; Dienstleder, M.; Poggio, M.; Matković, A. Imaging Magnetic Order in a Two-Dimensional Iron-Rich Phyllosilicate. *Commun. Mater.* **2025**, *6* (1), 217.
(32) White, A. F.; Brantley, S. L. The Effect of Time on the Weathering of Silicate Minerals: Why Do Weathering Rates Differ in the Laboratory and Field?. *Chem. Geol.* **2003**, *202* (3–4), 479–506.
(33) Irani-nezhad, M. H.; Khataee, A.; Orooji, Y.; Vatanpour, V.; Arefi-Oskoui, S. Fabrication of Two-Dimensional Biotite Nanosheets from Natural Biotite Clay as a Potent Antibacterial Agent. *Colloid. Surf., A* **2023**, *674*, 131905.
(34) Rezayani, M.; Sharif, F.; Makki, H. Understanding Ion Diffusion in Anion Exchange Membranes; Effects of Morphology and Mobility of Pendant Cationic Groups. *J. Mater. Chem. A* **2022**, *10* (35), 18295–18307.
(35) Zanazzi, P. F.; Pavese, A. Behavior of Micas at High Pressure and High Temperature. *Rev. Mineral. Geochem.* **2002**, *46*, 99–116.
(36) Wu, H.; Lin, S.; Cheng, X.; Chen, J.; Ji, Y.; Xu, D.; Kang, M. Comparative Study of Strontium Adsorption on Muscovite, Biotite and Phlogopite. *J. Environ. Radioact.* **2020**, *225*, 106446.
(37) Delley, B. From Molecules to Solids with the DMol3 Approach. *J. Chem. Phys.* **2000**, *113*, 7756–7764.
(38) Paier, J.; Hirschl, R.; Marsman, M.; Kresse, G. The Perdew-Burke-Ernzerhof Exchange-Correlation Functional Applied to the G2-1 Test Set Using a Plane-Wave Basis Set. *J. Chem. Phys.* **2005**, *122* (23), 234102.
(39) Perdew, J. P.; Burke, K.; Ernzerhof, M. Generalized Gradient Approximation Made Simple [Phys. Rev. Lett 77, 3865 (1996)]. *Phys. Rev. Lett.* **1997**, *78*, 1396.
(40) Tkatchenko, A.; Scheffler, M. Accurate Molecular van Der Waals Interactions from Ground-State Electron Density and Free-Atom Reference Data. *Phys. Rev. Lett.* **2009**, *102* (7), 073005.
(41) Ji, X.; Kang, Y.; Ouyang, J.; Chen, Y.; Artzi, D.; Zeng, X.; Xiao, Y.; Feng, C.; Qi, B.; Kim, N. Y.; Saw, P. E.; Kong, N.; Farokhzad, O. C.;

https://doi.org/10.1021/acsaelm.6c00747
ACS Appl. Electron. Mater. 2026, 8, 5750–5762

Tao, W. Synthesis of Ultrathin Biotite Nanosheets as an Intelligent Theranostic Platform for Combination Cancer Therapy. *Adv. Sci.* **2019**, *6* (19), 1901211.
(42) Wang, A.; Freeman, J. J.; Jolliff, B. L. Understanding the Raman Spectral Features of Phyllosilicates. *J. Raman Spectrosc.* **2015**, *46* (10), 829–845.
(43) Aseev, G. G.; Zaĭtsev, I. D. Volumetric Properties of Electrolyte Solutions: Estimation Methods and Experimental Data. *J. Am. Chem. Soc.* **1997**, *119* (50), 12423.
(44) Li, M.; Fan, Q.; Gao, L.; Liang, K.; Huang, Q. Chemical Intercalation of Layered Materials: From Structure Tailoring to Applications. *Adv. Mater.* **2024**, *36*, 2312918.
(45) Balachandran, C.; Muñoz, J. F.; Arnold, T. Characterization of Alkali Silica Reaction Gels Using Raman Spectroscopy. *Cem. Concr. Res.* **2017**, *92*, 66–74.
(46) Hobbs, C.; Jaskaniec, S.; McCarthy, E. K.; Downing, C.; Opelt, K.; Güth, K.; Shmeliov, A.; Mourad, M. C. D.; Mandel, K.; Nicolosi, V. Structural Transformation of Layered Double Hydroxides: An in Situ TEM Analysis. *npj 2D Mater. Appl.* **2018**, *2* (1), 4.
(47) Elmi, C.; Guggenheim, S.; Gieré, R. Surface Crystal Chemistry of Phyllosilicates Using X-Ray Photoelectron Spectroscopy: A Review. *Clays Clay Miner.* **2016**, *64*, 537–551.
(48) Sawyer, R.; Nesbitt, H. W.; Secco, R. A. High Resolution X-Ray Photoelectron Spectroscopy (XPS) Study of K 2O-SiO_2 Glasses: Evidence for Three Types of O and at Least Two Types of Si. *J. Non Cryst. Solids* **2012**, *358* (2), 290–302.
(49) Ji, X.; Ge, L.; Liu, C.; Tang, Z.; Xiao, Y.; Chen, W.; Lei, Z.; Gao, W.; Blake, S.; De, D.; Shi, B.; Zeng, X.; Kong, N.; Zhang, X.; Tao, W. Capturing Functional Two-Dimensional Nanosheets from Sandwich-Structure Vermiculite for Cancer Theranostics. *Nat. Commun.* **2021**, *12* (1), 1124.
(50) Usler, A. L.; Ketter, F.; Souza, R. A., De How Space-Charge Behaviour at Grain Boundaries in Electroceramic Oxides Is Modified by Two Restricted Equilibria. *Phys. Chem. Chem. Phys.* **2024**, *26* (10), 8287–8298.
(51) Demirezen, S.; Kaya, A.; Yerişkin, S. A.; Balbaşi, M.; Uslu, I. Frequency and Voltage Dependent Profile of Dielectric Properties, Electric Modulus and Ac Electrical Conductivity in the PrBaCoO Nanofiber Capacitors. *Results Phys.* **2016**, *6*, 180–185.
(52) Klahr, B.; Gimenez, S.; Fabregat-Santiago, F.; Bisquert, J.; Hamann, T. W. Photoelectrochemical and Impedance Spectroscopic Investigation of Water Oxidation with "Co-Pi"-Coated Hematite Electrodes. *J. Am. Chem. Soc.* **2012**, *134* (40), 16693–16700.
(53) Zi, Y.; Wang, J.; Wang, S.; Li, S.; Wen, Z.; Guo, H.; Wang, Z. L. Effective Energy Storage from a Triboelectric Nanogenerator. *Nat. Commun.* **2016**, *7*, 10987.
(54) Chen, X.; Lou, Z.; Gao, X.; Yin, L.; Qin, S.; Lin, M.; Zhang, F.; Lu, Y.; Ding, S.; Liu, R.; Tang, S.; Zhou, S.; Dang, D. T.; Yang, X.; Wu, Z.; Zhang, Z.; Hu, H.; Wang, X.; Zhu, Y.; Xu, Y.; Sheng, R.; Zhou, J.; Lu, C.; Wang, R.; Yue, W.; Huang, H.; Wu, R. S.; Bian, Y.; Park, G.; Cao, J.; Liu, X.; Luo, D.; Cauwenberghs, G.; Wang, J.; Xu, S. A Noise-Tolerant Human–Machine Interface Based on Deep Learning-Enhanced Wearable Sensors. *Nature Sensors* **2025**, *1*, 39.
(55) Scott, A. D.; Smith, S. J. Susceptibility of interlayer Potassium in Micas to Exchange with Sodium. *Clays Clay Miner.* **1966**, *14*, 69–81.
(56) Saltas, V.; Pentari, D.; Vallianatos, F. Complex Electrical Conductivity of Biotite and Muscovite Micas at Elevated Temperatures: A Comparative Study. *Materials* **2020**, *13* (16), 3513.
(57) Zhu, G.; Pan, C.; Guo, W.; Chen, C. Y.; Zhou, Y.; Yu, R.; Wang, Z. L. Triboelectric-Generator-Driven Pulse Electrodeposition for Micropatterning. *Nano Lett.* **2012**, *12* (9), 4960–4965.
(58) Zhao, Z.; Zhou, L.; Li, S.; Liu, D.; Li, Y.; Gao, Y.; Liu, Y.; Dai, Y.; Wang, J.; Wang, Z. L. Selection Rules of Triboelectric Materials for Direct-Current Triboelectric Nanogenerator. *Nat. Commun.* **2021**, *12* (1), 4686.
(59) Cheng, L.; Xu, Q.; Zheng, Y.; Jia, X.; Qin, Y. A Self-Improving Triboelectric Nanogenerator with Improved Charge Density and Increased Charge Accumulation Speed. *Nat. Commun.* **2018**, *9* (1), 3773.

https://doi.org/10.1021/acsaelm.6c00747
ACS Appl. Electron. Mater. 2026, 8, 5750–5762